Science of the Total Environment 644 (2018) 439–451

Contents lists available at ScienceDirect

Science of the Total Environment

journal homepage: www.elsevier.com/locate/scitotenv

Seasonal patterns of canopy photosynthesis captured by remotely sensed sun-induced fluorescence and vegetation indexes in mid-to-high latitude forests: A cross-platform comparison

Xinchen Lu [a], Xiao Cheng [a,b,*], Xianglan Li [a,b,*], Jiquan Chen [c], Minmin Sun [a], Ming Ji [a], Hong He [a], Siyu Wang [a], Sen Li [a], Jianwu Tang [d]

[a] *State Key Laboratory of Remote Sensing Science, College of Global Change and Earth System Science, Beijing Normal University, Beijing 100875, China*
[b] *Joint Center for Global Change and China Green Development, Beijing Normal University, Beijing 100875, China*
[c] *College of Social Science, Department of Geography, Michigan State University, East Lansing, MI, USA*
[d] *The Ecosystems Center, Marine Biological Laboratory, Woods Hole, MA, USA*

HIGHLIGHTS

- Phenological metrics from 2 SIF sets and 4 vegetation indexes were intercompared.
- Remotely sensed SIF were highly correlated with GPP in mid-to-high latitude forests.
- The SIF-GPP relationships can be generally considered linear at 16-day scale.
- PI and NDVI provided reliable predictions of start of seasons among MODIS indexes.
- Limitations remained for OCO-2 SIF to extract photosynthesis phenology at site-level.

GRAPHICAL ABSTRACT

The original EC GPP and OCO-2 SIF with the fitted seasonal cycles and predicted SOS and EOS at six forested sites.

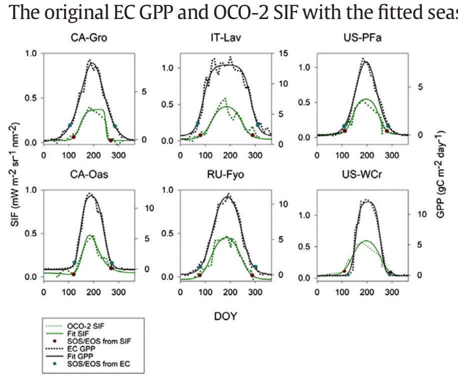

ARTICLE INFO

Article history:
Received 19 April 2018
Received in revised form 19 June 2018
Accepted 21 June 2018
Available online 11 July 2018

Editor: Elena PAOLETTI

Keywords:
Phenology
Remote sensing
Photosynthesis
OCO-2
Sun-induced fluorescence
Vegetation indexes

ABSTRACT

Characterized by the noticeable seasonal patterns of canopy photosynthesis, mid-to-high latitude forests are sensitive to climate change and crucial for understanding the global carbon cycle. To monitor the seasonal cycle of the canopy photosynthesis from space, several remotely sensed indexes, such as normalized difference vegetation index (NDVI), enhanced vegetation index (EVI), and leaf area index (LAI) have been implemented within the past decades. Recently, satellite-derived sun-induced fluorescence (SIF) has shown great potential of providing retrievals that are more related to photosynthesis process. However, the potentials of different canopy measurements have not been thoroughly assessed in the context of recent advances of new satellites and proposals of improved indexes. At 15 forested sites, we present a cross-platform intercomparison of one emerging remote sensing based index of phenology index (PI) and two SIF datasets against the conventional indexes such as NDVI, EVI, and LAI to capture the seasonal cycles of canopy photosynthesis. NDVI, EVI, LAI, and PI were calculated from Moderate Resolution Imaging Spectroradiometer (MODIS) measurements, while SIF were evaluated from Global Ozone Monitoring Experiment-2 (GOME-2) and Orbiting Carbon Observatory-2 (OCO-2) observations. Results indicated that GOME-2 SIF was highly correlated with gross primary production (GPP) and absorbed photosynthetically active radiation during the growing seasons. The SIF-GPP relationship can generally be considered linear at the 16-day scale. Key phenological metrics such as start of the seasons and end of the seasons captured

* Corresponding authors at: State Key Laboratory of Remote Sensing Science, College of Global Change and Earth System Science, Beijing Normal University, Beijing 100875, China.
E-mail addresses: xcheng@bnu.edu.cn (X. Cheng), xlli@bnu.edu.cn (X. Li).

https://doi.org/10.1016/j.scitotenv.2018.06.269

by SIF from GOME-2 and OCO-2 matched closely with photosynthesis phenology as inferred by GPP. However, the applications of OCO-2 SIF for phenological studies may be limited only for a small range of sites (at site-level) due to a limited spatial sampling. Among the MODIS estimations, PI and NDVI provided most reliable predictions of start of growing seasons, while no indexes accurately captured the end of growing seasons.

1. Introduction

Terrestrial ecosystems play an important role in regulating regional and global climate (Burrows et al., 2011). Mid-to-high latitude forests, especially the boreal forests, are substantial contributors to carbon fluxes (Beer et al., 2010; Rolleston, 1996). As plants in these regions are expected to experience the greatest warming among forest biomes, they are deemed to react and respond sensitively to climate change and variability (Keenan et al., 2014). In recent years, with the developments of networks of flux measurements and advances of remote sensing based models, the monitoring of the physiological processes such as photosynthesis of mid-to-high latitudes has become generally possible.

Mid-to-high latitude forests are showing noticeable seasonal cycles of canopy photosynthesis. These life cycle events are sensitive indicators of the biosphere's response to climate changes through contributions to the global carbon, energy and water cycles (Buitenwerf et al., 2015; Peñuelas et al., 2009). Understanding the changes of these cycles as well as the underlying mechanisms are of significance for predicting future changes of climate and the global carbon cycle. Recent in-situ and remote sensing based studies have shown that the warming climate has triggered lengthier growing seasons in northern hemisphere regions (Cleland et al., 2007; Viña et al., 2016; Wang et al., 2015). Remote sensing based approaches to estimate phenological metrics (e.g., the start and end of growing seasons) were mainly based on reflectance-calculated vegetation indexes (VIs), such as normalized difference vegetation index (NDVI), enhanced vegetation index (EVI) and leaf area index (LAI) retrieved using these VIs (Helman, 2018). These indexes have been applied to regional and global studies, especially for the regions without long-term ground observations (Gonsamo and Chen, 2016). Fundamentally, yet, those VIs cannot provide us a direct understanding of physiological processes so that can be hard to be perfectly applied to modelling frameworks. At the same time, several recent studies found that performances of VIs are significantly hindered by snow cover and soil moisture in high-latitude regions (D'Odorico et al., 2015; Peng et al., 2017; Wu et al., 2017). Several improved indexes including phenology index (PI) that aimed at the match between remotely sensed and ground observed seasonal cycles of canopy photosynthesis have been proposed in recent years (Gonsamo et al., 2012a). The PI combines NDVI and Normalized Difference Infrared Index (NDII) aiming to decouple the seasonality of the green vegetation component from the background one because green-up co-occurs with snow melt (Delbart et al., 2005; Gonsamo et al., 2012a). Yet, the biological recovery and dormancy for evergreen forests are still extremely difficult to identify during the transition period when the greenness signal of the vegetation is weak or does not necessarily correspond with the shifts of photosynthesis (Wong and Gamon, 2015).

Fortunately, recent advances of atmospheric measurements has made it possible to retrieve an alternative indicator that is more related to the photosynthesis processes: sun-induced fluorescence (SIF). Chlorophyll pigments absorb photons to power photosynthesis, with some of the photons are re-emitted at longer wavelengths as chlorophyll fluorescence (Baker, 2008). The re-emitted SIF has been successfully related to downward carbon flux, i.e., carbon uptake by the vegetation. This provides a promising way in estimating photosynthesis through SIF. Global SIF datasets using space-borne spectroscopy from satellites became available past few years (Frankenberg et al., 2011; Frankenberg et al., 2014; Guanter et al., 2013; Guanter et al., 2014; Joiner et al., 2013; Joiner et al., 2016; Köhler et al., 2015). Despite the complex processes underlying the relationship between SIF and gross primary production (GPP), it has been reported the satellite-retrieved SIF was highly correlated with GPP estimated based on eddy covariance (EC) flux towers (van der Tol et al., 2014; Verma et al., 2017; Yang et al., 2017; Yang et al., 2015; Zhang et al., 2016b). Their relationship appears to reflect the level of absorbed photosynthetically active radiation (APAR) with additional information of light use efficiency (LUE). Based on >50 EC towers, Joiner et al. (2014) found that the Global Ozone Monitoring Experiment-2 (GOME-2) SIF retrieved phenological metrics matched closely with that of EC-based estimations, although the footprints of GOME-2 (40 km by 80 km) were significantly larger than most EC sites. Walther et al. (2016) found that GOME-2 SIF decoupled growing seasons can be up to 6 weeks longer than that captured by EVI. Jeong et al. (2017) evaluated remotely sensed SIF and NDVI of several platforms and proposed that the continued measurements of SIF and NDVI would help us to understand the seasonal variations of vegetation photosynthesis and greenness. However, the coarse spatial representativeness of previous atmospheric measurements (~40 km by 80 km or coarser) makes it difficult to compare with ground-based canopy measurements (Chen et al., 2012; Joiner et al., 2014; Zhang et al., 2016b). Very recently, Orbiting Carbon Observatory 2 (OCO-2) has shown renewed promises of provinding satellite-derived SIF with the improved spatial representativeness at around 1.3 km by 2.25 km (Frankenberg et al., 2014). The footprints of OCO-2 that match the spatial representativeness of most EC towers enables it to produce better results (Lu et al., 2018; Verma et al., 2017). The emerging observations from OCO-2, however, have rarely been applied in phenological studies (Köhler et al., 2018).

In most physiological models, VIs and/or LAI were used to decouple the seasonal cycles of processes such as photosynthesis (Wang et al., 2016). To constrain the uncertainties of current models regarding the estimations of productivity, the use of high-resolution and global retrieval of SIF might further improve the accuracy. In the context of extreme events including prolonged droughts in recent decades, it was vital to comprehensively investigate the usability of SIF in monitoring canopy photosynthesis, including the key phenological metrics, compared with conventional VIs and LAI (Dahlin et al., 2015; Melaas et al., 2016; Zipper et al., 2016). At the same time, although several models that can estimate GPP globally with VIs have been proposed, the advantages of SIF can potentially be exploited to improve their performances especially at high-latitude regions (Jeong et al., 2017; Luus et al., 2017; Luus and Lin, 2015). However, the advantages of SIF compared against conventional VIs have not been comprehensively accessed in the context that there are advances of new satellites capable of monitoring SIF at relatively high spatial resolutions and proposal of improved VIs with different theories (Sun et al., 2017). In this study, our primary objective was to evaluate and compare the seasonal cycles of several remotely sensed canopy measurements across mid-to-high latitude forests with a focus on evergreen needleleaf forests (ENF), deciduous broadleaf forests (DBF) and mixed forests (MF). An additional objective was to focus on phenological transition dates derived from different platforms, which are indicators directly related to the carbon budgets of terrestrial ecosystems.

2. Materials and methods

2.1. EC estimated canopy properties

We conducted this study at 15 EC sites in North America and Europe where relatively homogeneous landscapes exist around the flux towers.

In total, there are 103 site-years with a mean of 6.9 years of observations for each site. These sites represent three main forest biomes in mid-to-high latitude forests such as ENF, DBF andMF (Fig. 1 and Table 1). The selection of EC sites was based on an assumption of threshold (60%) of International Geosphere-Biosphere Program (IGBP) classifications (Loveland et al., 2000). To be specific, we chose sites where >60% of the GOME-2 grid areas around each flux tower matched with the biome for the corresponding site. MODIS land cover products (MCD12Q1) and one previous study on several homogeneous sites were used as references for our site selection (Zhang et al., 2016a). In some sites, if the site is dominated by ENF (or DBF) pixels but surrounded by some MF pixels, we do not distinguish the ENF (or DBF) pixels and MF pixels as long as the sum of them exceeded 60% of whole grid areas of GOME-2 (Zhang et al., 2016a). EC measurements were downloaded from the European Fluxes Database Cluster (http://gaia.agraria.unitus.it/) and Fluxnet (http://fluxnet.fluxdata.org/).

In both datasets, we used the gap-filled (based on marginal distribution sampling) estimations provided by both data sources including air temperature, downward shortwave radiation (SWIN) and CO_2 fluxes (Baldocchi et al., 2001). The daily composites were then attributed every 8 days with an average over the 16-day period. Quality flags and/or standard errors were screened for all analysed parameters to ensure that only the most reliable estimations remained. Photosynthetically active radiation (PAR) was calculated as 0.45 of SWIN for all sites (Jin et al., 2015). To partition net ecosystem exchange (NEE) into GPP and ecosystem respiration, we followed the night-time partitioning method (Reichstein et al., 2005). Since most sites did not provide measurements of APAR, we used MODIS Fraction of Photosynthetically

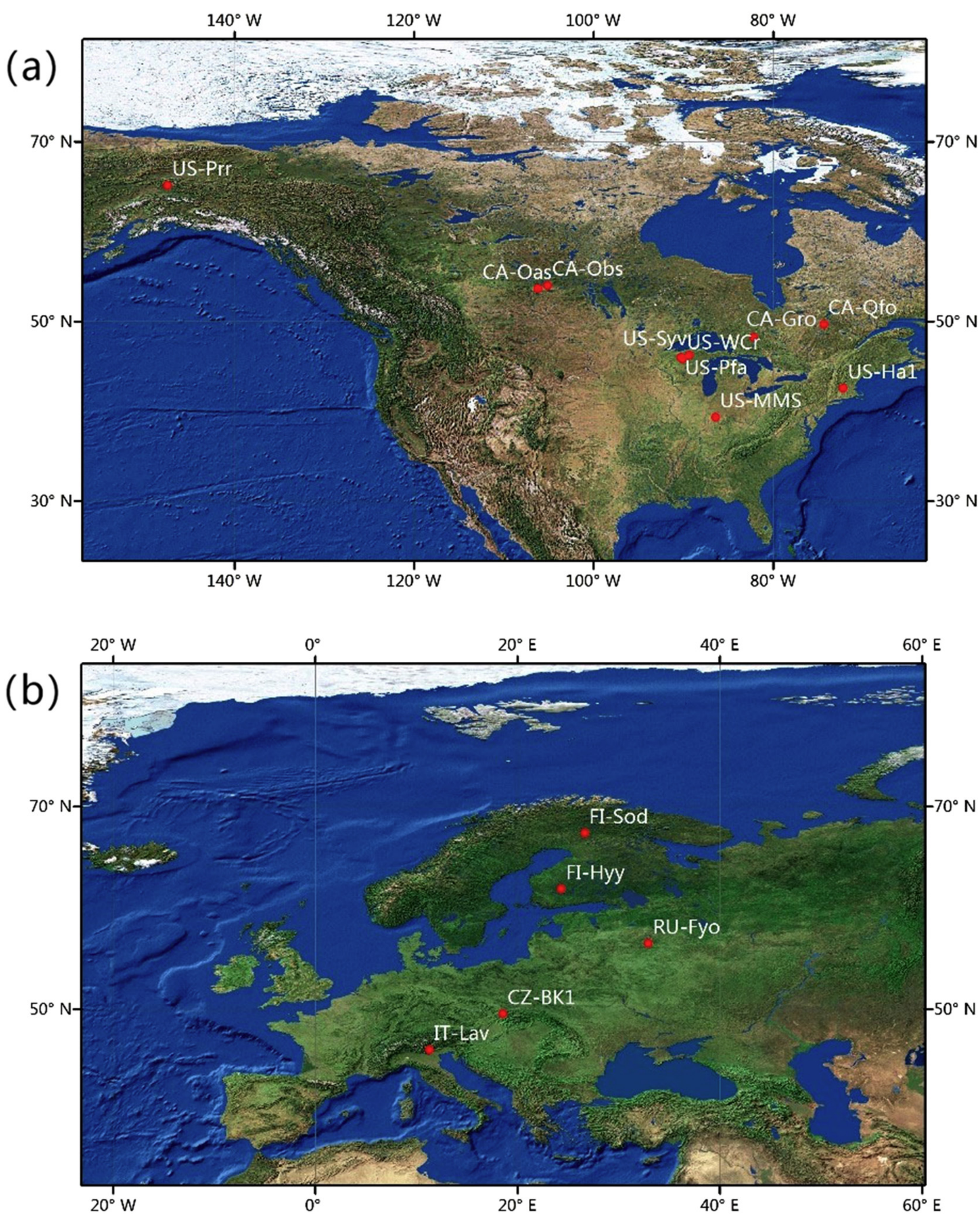

Fig. 1. Spatial distributions of the 15 mid-to-high latitude forests in North America (a) and Europe (b). The figure was generated using ArcMap 10.2 (http://www.esri.com/).

Table 1
Basic information and descriptions of EC flux sites. Among all sites, eddy measurements of sites CZ-BK1, DK-Sor, FI-Sod, IT-Lav, and RU-Fyo were downloaded from the European Fluxes Database Cluster, while measurements from other sites were obtained from the FLUXNET. Year denotes the corresponding time of the measurements, Type indicates land cover type, and Max_LC is the percent of dominant vegetation cover within the GOME-2 grid calculated for each site. OCO-2 indicates whether this site was selected for comparisons with OCO-2 measurements.

Site	Lat.	Lon.	Site name	Year	Type	Max_LC	OCO-2	References
CA-Gro	48.2167	−82.1556	Canada-Ontario 4	2007–2014	MF	90	Yes	Mccaughey et al. (2006)
CA-Oas	53.6289	−106.1978	SK-Old Aspen	2007–2010	DBF	60	Yes	Barr et al. (2002)
CA-Obs	53.9872	−105.1178	SK-Southern Old Black Spruce	2007–2010	ENF	88	No	Bond-Lamberty et al. (2004)
CA-Qfo	49.6925	−74.3421	Eastern Boreal, Mature Black Spruce	2007–2010	ENF	71	No	Bergeron et al. (2007)
CZ-BK1	49.5021	18.5369	Bily Kriz-Beskidy Mountains	2007–2014	DBF	60	No	Staudt and Foken (2008)
FI-Hyy	61.8475	24.295	Finland-Hyytiala	2007–2014	ENF	93	No	Suni et al. (2003)
FI-Sod	67.3619	26.6378	Sodankyla	2007–2014	ENF	99	No	Tanja et al. (2003)
IT-Lav	45.9562	11.2813	Italy-Lavarone	2007–2014	ENF	60	Yes	Marcolla et al. (2003)
RU-Fyo	56.4615	32.9221	Russia-Fyodorovskoye dry spruce	2007–2014	ENF	95	Yes	Milyukova et al. (2002)
US-Ha1	42.5378	−72.1715	Harvard Forest EMS Tower (HFR1)	2007–2012	DBF	91	No	Urbanski et al. (2007)
US-MMS	39.3232	−86.4131	Morgan Monroe State Forest	2007–2014	DBF	91	No	Dragoni et al. (2011)
US-PFa	45.9459	−90.2723	USA-Park Falls	2007–2017	MF	78	Yes	Desai (2014)
US-Prr	65.1237	−147.4876	Poker Flat Res. Range Black Spruce	2010–2014	ENF	87	No	Nakai et al. (2013)
US-Syv	46.242	−89.3477	USA-Sylvania Wilderness Area	2007–2008, 2012–2014	MF	93	No	Desai et al. (2005)
US-WCr	45.8059	−90.0799	USA-Willow Creek	2010–2017	DBF	95	Yes	Cook et al. (2004)

Active Radiation (FPAR) products (will be introduced in Section 2.3) to estimate APAR as MODIS FPAR × PAR. At the same time, since several previous study pointed out EVI outperformed the MODIS FPAR products in estimating APAR, we referred to EVI × PAR as an alternative estimate of APAR (Liu et al., 2017; Sims et al., 2008).

In addition to site level flux data, we used FLUXCOM data in our comparison (Jung et al., 2009; Tramontana et al., 2016). This dataset is a machine learning based re-analysis of flux data in combination with remote sensing and meteorological data to upscale flux tower point estimates to a global scale with similar spatial representativeness (0.5°) of GOME-2 SIF products (Tramontana et al., 2016). We averaged the outcomes of six algorithms, i.e., three machine-learning algorithms (random forest, artificial neural network and multivariate adaptive regression splines) by two partitioning methods, and then attributed the composites every 8 days with an average over the 16-day period.

2.2. Satellite-derived SIF

We used satellite-derived SIF data derived from the GOME-2 instrument on-board MetOp-A platform (ftp://fluo.gps.caltech.edu/data/Philipp/GOME-2) which initially measured backscattered sunlight at wavelengths between 270 and 790 nm in four separate channels. Its fourth channel (590–790 nm) encompassed a range of wavelengths of emitted SIF. This GOME-2 SIF dataset used a linear method to retrieve SIF at 740 nm (Köhler et al., 2015). The SIF dataset was gridded with a spatial resolution of 0.5° after normalizing to the daily averages. Similar to the pre-processing of EC variables, we averaged the daily retrievals of SIF every 8 days with an average over the 16-day period. We also applied the remotely sensed fluorescence from OCO-2 that was launched on July 2, 2014. The relatively small footprints of instruments of OCO-2 (~1.3 km by 2.25 km) made it possible to produce the first satellite-derived SIF dataset that better matches the EC-based estimations. OCO-2 has spectrally highly resolved measurements in the O_2 A-band and is capable of retrieving SIF centred at 757 nm and 771 nm accurately (Frankenberg et al., 2014). The SIF at 771 nm is relatively weaker than that at 757 nm, thus we averaged the records of two bands after scaling the values at 771 nm with a factor of 1.4 (Verma et al., 2017). In this study, the search radius of OCO-2 SIF data was set at 10 km following the similar protocols of Verma et al. (2017) and Luus et al. (2017). One of the advantages of OCO-2 SIF, at the same time, is that it enables the comparison between satellite-derived SIF and tower GPP at instantaneous scale due to its relatively fine resolution and capacity to retrieve SIF at a short period of time (Sun et al., 2018; Verma et al., 2017).

There are several differences between satellite-derived SIF from the two instruments. Firstly, the retrieved SIF is centred at 740 nm for GOME-2 and 757 nm (771 nm) for OCO-2, respectively. Secondly, unlike the global continuous measurements of GOME-2, the strategy of spatial sampling of OCO-2 is sparse, with only a few sites in this study to have sufficient times of observations that can be used to quantify the seasonal patterns. Additionally, the overpass times of the two satellites differ from each other, i.e., morning for GOME-2 and noon for OCO-2. As a result, only 6 EC sites with most observations from OCO-2 were selected for comparisons (Table 1). For OCO-2 SIF, when compared with GOME-2 SIF or daily EC measurements, we used the daily correction factor provided within the files to convert the instantaneous values to daily averages. Meanwhile, the measurements of FLUXNET and European Flux Data Cluster only updated to 2014 for most sites. Thus, for US-PFa and US-WCr, we requested the EC estimations up to 2017 from their website (http://flux.aos.wisc.edu/twiki/bin/view/Main/ChEASData). For other sites, we merged the values from OCO-2 from late 2014 to 2016 into a year to reconstruct the time series of a year by the corresponding day of the year of the measurements to compare with EC-based estimations in 2014.

2.3. Surface reflectance and FPAR/LAI

To calculate NDVI, EVI and PI, bidirectional reflectance distribution function (BRDF) adjusted surface reflectance derived from the MODIS instruments were obtained from Oak Ridge National Laboratory's Distributed Active Archive Center (MCD43A4, V005, with a spatial resolution of 500 m, combined from Terra and Aqua) (Attard et al., 2016). In this data set, the values of reflectance were normalized to nadir, cloud-free, atmospherically corrected estimations based on the BRDF, and were attributed into a 16-day series with a sampling of every 8 days. The MCD43 series data sets used a separate product (MCD43A2) in simplified form to store quality information. The layer of "BRDF_Albedo_Quality" indicated the quality of the BRDF-adjusted reflectance. We only used the measurements labelled as "best" and "good" in quality.

We used the level 4 product of FPAR and LAI from the Oak Ridge National Laboratory's Distributed Active Archive Center (MOD15A2, V005, with a spatial resolution of 1000 m, from MODIS Terra) (Fretwell et al., 2012; Myneni et al., 2002). For product MOD15A2, retrievals were targeted towards consistency with field measurements over all biomes but with a major focus on woody vegetation. In summary, all datasets used in this study are listed (Table 2).

2.4. Computations of vegetation indexes and phenology indexes

The red, blue, near-infrared and shortwave-infrared surface reflectance from the MCD43A4 product with the exact acquisition dates were used to compute the EVI, NDVI, NDII and PI. NDII responds to

Table 2
A summary of all datasets used in this study. The description, size of footprint, period and references are listed.

Dataset	Description	Footprint	Period	References
Fluxnet 2015	Flux measurements at multiple sites	Typically 500 m to 1 km	2007–2014	Baldocchi et al. (2001)
European Flux Database Cluster	Flux measurements at multiple European sites	Typically 500 m to 1 km	2007–2014	http://www.europe-fluxdata.eu/
Fluxcom	An upscaled modelling GPP data set	0.5°	2007–2013	Jung et al. (2011)
GOME-2 SIF	Satellite-derived SIF from GOME-2	40 km by 80 km	2007–2014	Köhler et al. (2015)
OCO-2 SIF	Satellite-derived SIF from OCO-2	1.3 × 2.25 km	2014–2016	Frankenberg et al. (2014)
MOD15A2	Level 4 product of FPAR & LAI	1 km	2007–2014	Myneni et al. (2002)
MCD43A4	MODIS Nadir BRDF-Adjusted Reflectance surface reflectance	500 m	2007–2014	Attard et al. (2016)

land surface moisture and snow cover and can thus capture the seasonal trajectories of snow cover. The EVI, NDVI and NDII were calculated as (Gonsamo et al., 2012b; Huete et al., 2002):

$$\mathrm{EVI} = 2.5 \times \frac{\rho_{nir} - \rho_{red}}{\rho_{nir} + (6 \times \rho_{nir} - 7 \times \rho_{blue}) - 1} \tag{1}$$

$$\mathrm{NDVI} = \frac{\rho_{nir} - \rho_{red}}{\rho_{nir} + \rho_{red}} \tag{2}$$

$$\mathrm{NDII} = \frac{\rho_{nir} - \rho_{SWIR}}{\rho_{nir} + \rho_{SWIR}} \tag{3}$$

where ρ_{nir}, ρ_{SWIR}, ρ_{red} and ρ_{blue} represent reflectance at near-infrared, shortwave infrared, red and blue bands, respectively. Then, NDVI and NDII were integrated to calculate PI. The PI was derived from the product of the sum and the difference of NDVI and NDII as (Delbart et al., 2005; Gonsamo et al., 2012a):

$$\mathrm{PI} = \begin{cases} 0, & if\ NDVI<0\ or\ NDII<0 \\ (NDVI + NDII) \times (NDVI - NDII) & \\ 0, & if\ PI<0 \end{cases} \tag{4}$$

2.5. The linear model and hyperbolic model for illustrating the SIF-GPP relationship

The relationship between SIF and canopy photosynthesis can be complex, several previous studies pointed out that their relationship can be nonlinear at instantaneous scale (Damm et al., 2010; Damm et al., 2015; Li et al., 2018; Yang et al., 2016; Zhang et al., 2016a). Damm et al. (2015) and Li et al. (2018) proposed that a hyperbolic model may outperform the linear model when analysing the relationship between SIF and GPP. In this study, we used the linear model as well as the hyperbolic (nonlinear) model to analyse the relationship between SIF and GPP. The hyperbolic model assumed that the SIF-GPP relationship can be nonlinear as LUE can be expressed by a hyperbolic function of APAR. This simplified model can be expressed as follow (Li et al., 2018):

$$\mathrm{GPP} = GPP_{max} \times \frac{SIF}{SIF + b} \tag{5}$$

$$SIF_{yield} = \frac{SIF}{APAR} \tag{6}$$

where $\mathrm{GPP}_{\mathrm{max}}$ represents the maximum of a GPP dataset that can be set accordingly and b was a parameter related to $\mathrm{SIF}_{\mathrm{yield}}$ that needs to be determined by nonlinear fitting.

2.6. Determinations of phenological metrics

We used the curve fitting method to objectively determine phenological metrics (Gonsamo et al., 2012b).

$$X(t) = a1 + \frac{a2}{1 + \exp(-d1(t - b1))} - \frac{a3}{1 + \exp(-d2(t - b2))} \tag{7}$$

Eq. (7) was fitted to all measurements, where $X(t)$ is the input time series (e.g., GOME-2 SIF), and $a1$, $a2$, $a3$, $b1$, $b2$, $d1$, and $d2$ are the empirical coefficients to be determined. Weighting-scheme based least-squares curve fitting was applied by starting from a first guess of the

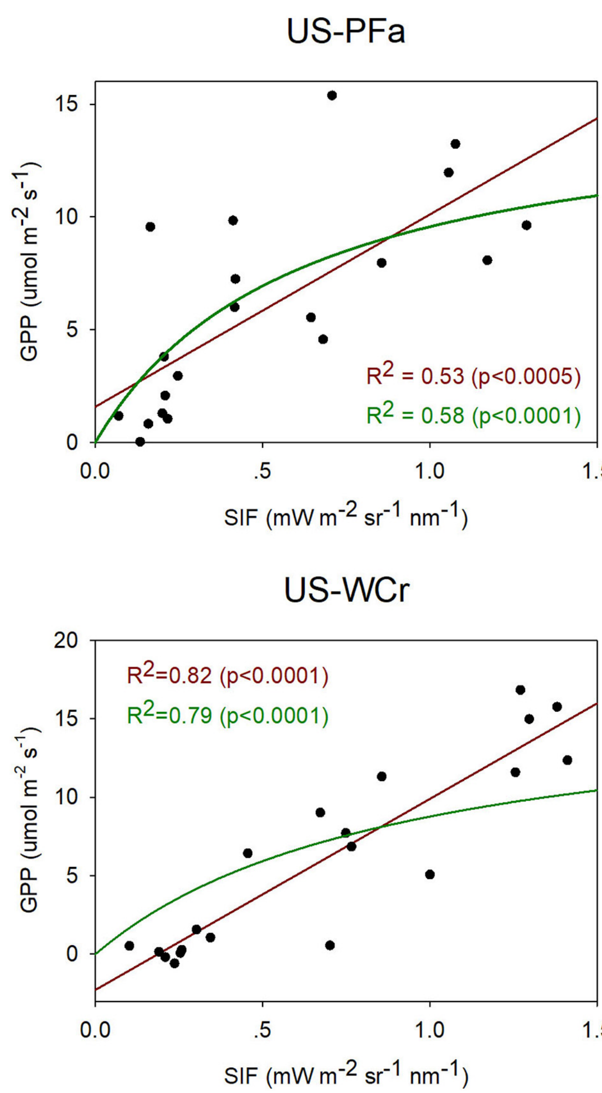

Fig. 2. The relationship between OCO-2 SIF and GPP at US-PFa and US-WCr at instantaneous scale.

seven functions and solving with a maximum of 2000 iterations. A three-point moving window approach was used to reduce the effect of low-quality data points by assigning the values less than half or more than twice of its associated median values with lower weights. For NDVI, we referred to the midpoints of b1 and b2 as the start of seasons (SOS) and end of seasons (EOS) as previous studies found that the midpoint-days of NDVI were strongly connected with leaf-unfolding process for deciduous forests in North America and China (Luo et al., 2014). For other observations, the phenological metrics were determined as:

$$SOS = b1 - \frac{4.562}{2d1} \tag{8}$$

$$EOS = b2 + \frac{4.562}{2d2} \tag{9}$$

In principle, this method tried to find the inflection point within the time series. The value of 4.562 was the solution that Gonsamo et al. (2012a) found and then has been applied in several studies (D'Odorico et al., 2015; Walther et al., 2016). Because of the limited observations of OCO-2 SIF, it can be problematic to retrieve 7 free parameters. In theory, VIs may rest at different values during the non-growing seasons at different years due to the differences of backgrounds each year. MODIS LAI may as well be affected since it was retrieved with the use of those VIs, but SIF should not be affected and should be very close to 0 during non-growing seasons. Thus, we simplified the models by using the same value for a2 and a3 when analysing time series of OCO-2 SIF.

3. Results

3.1. Relationship between satellite-derived SIF and EC towers based GPP

We used the OCO-2 SIF to explore the relationship of satellite-derived SIF and GPP at instantaneous scale at US-PFa and US-WCr first (Fig. 2). The EC instruments of US-PFa and US-WCr were located in a mixed forest and a deciduous forest in northern Wisconsin, USA, respectively. From late 2014 to 2017, there were 21 times of observations from OCO-2 at US-PFA and 20 times of observations at US-WCr. At both sites, the correlations of linear and hyperbolic models were statistically significant ($p < 0.0005$). In US-PFa, the performance of linear model ($R^2 = 0.53$, $p < 0.0005$) was slightly worse than the hyperbolic model ($R^2 = 0.58$, $p < 0.0001$). In US-WCr site, interestingly, the performances of both models were similar, with R^2 of 0.82 for the linear model and 0.79 for the hyperbolic model, respectively ($p < 0.0001$ in both models).

Then, we moved on to test the relationship between GOME-2 SIF and EC tower based GPP on 16-day scale. Results indicated that all the

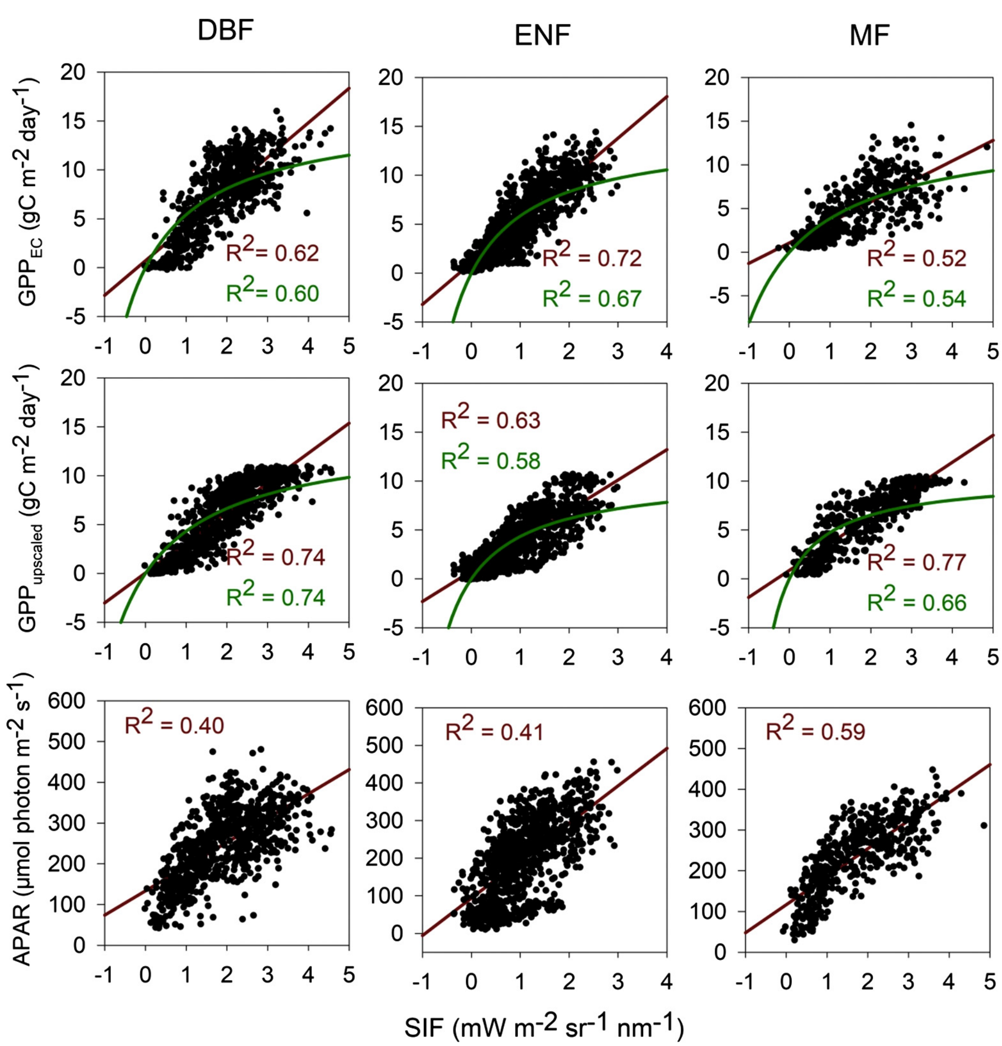

Fig. 3. Seasonal correlations between GOME-2 SIF and canopy photosynthesis in different forest biomes such as DBF, ENF, and MF. The red line represents the linear model, while the green line shows the hyperbolic model. The coefficients of determination of linear (red texts) and hyperbolic models (green texts) are remarked. All the correlations were statistically significant ($p < 0.0001$).

correlations were statistically significant ($p < 0.0001$). The relationship between GOME-2 SIF and canopy photosynthesis during the growing seasons was explored firstly through linear regression analysis (Fig. 3). We found that the seasonal patterns of SIF correlated highly with EC-based estimations of GPP (GPP_{EC}), with the correlation coefficient of determination (R^2) ranged from 0.52 to 0.72 ($R^2 = 0.62$, 0.72 and 0.52 for DBF, ENF and MF respectively). The GOME-2 SIF and upscaled GPP ($GPP_{upscaled}$) have similar spatial representativeness with relatively higher average R^2 values ranging from 0.63 to 0.77 ($R^2 = 0.74$, 0.63 and 0.77 for DBF, ENF and MF respectively). The GOME-2 SIF correlated well with APAR of MODIS FPAR×PAR, with the R^2 ranging from 0.40 to 0.59 ($R^2 = 0.40$, 0.41 and 0.59 for DBF, ENF and MF respectively). We also applied the hyperbolic model to estimate the relationship between GOME-2 SIF and canopy photosynthesis. In our cases, interestingly, the hyperbolic did not outperform the linear model generally with the R^2 ranging from 0.54 to 0.67 when fitting with GPP_{EC} and R^2 ranging from 0.58 to 0.74 when fitting with $GPP_{upscaled}$. The coefficients of determination showed a difference of 0.02 to 0.11 between two models. When fitting with GPP_{EC}, only in MF, the use of hyperbolic model slightly outperformed the linear model. And when compared with $GPP_{upscaled,}$ the hyperbolic models did not yield better predictions in any forest types. Although there seemed to be statuation effects on the relationship between GOME-2 SIF and $GPP_{upscaled}$ in DBF and MF.

The seasonal trajectories of SIF, GPP_{EC}, PAR, APAR, and EVI × PAR with averaged and normalized values of four sites were shown (Fig. 4). The seasonal cycles of other sites were presented in Fig. S1. Results indicated that PAR was already at relatively high level before the SOS of SIF and GPP_{EC}. SIF and GPP_{EC} showed similar time of spring onset and autumn senescence/abscission. However, APAR had relatively different seasonal trajectories from SIF and GPP_{EC}, with an earlier spring onset. For autumn senescence/abscission, SIF, GPP_{EC}, and APAR seemed to cease at a similar time (e.g., CA-Oas and CA-Obs). As mentioned, we used an alternative method to quantify APAR based on MODIS-derived EVI (Liu et al., 2017; Xiao et al., 2004a; Xiao et al., 2004b). This method used EVI to estimate the seasonal cycles of chlorophyll absorbed PAR. We found that EVI × PAR showed a seasonal cycle that was more consistent with GPP_{EC} and SIF (e.g., US-Syv).

3.2. Phenological metrics captured by different satellites

Results indicated that SOS and EOS derived using VIs, LAI and SIF were comparable but not equivalent (Figs. 5 and 6). For both the start and end of growing seasons, GOME-2 SIF provided the most reliable estimations, with the highest R^2 (0.67 for SOS and 0.52 for EOS) and lowest RMSEs (12.36 days for SOS and 11.64 days for EOS). For the other four MODIS based indexes, the remotely sensed phenological metrics and EC estimated seasonal cycles showed weaker correlations, with the overall $R^2 < 0.4$. For delineating the start of growing seasons, MODIS NDVI and PI had most accurate predictions (R^2 were 0.46 and 0.43 respectively). Other MODIS based indexes showed less promising results, with an overall R^2 below 0.3 ($R^2 = 0.20$ and 0.35 for EVI and LAI respectively). For autumn onset, the remotely sensed vegetation indexes seemed to be hindered, with the R^2 of <0.1 for MODIS NDVI, and R^2 of <0.4 for other indexes ($R^2 = 0.33$, 0.31 and 0.28 for EVI, PI and LAI respectively).

In DBF, GOME-2 SIF tracked the spring onset and autumn senescence/abscission accurately (Fig. 7). Both GOME-2 SIF and EC based estimations of GPP_{EC} showed that the growing seasons started from early-to-middle April and ceased in late October, with PI and NDVI tended to predict longer growing seasons. Meanwhile, EVI seemed to predict later EOS. In ENF, SIF produced a later spring onset by a few weeks but tracked the autumn senescence/abscission accurately. The PI and NDVI seemed to match the growing seasons, while EVI predicted longer growing seasons. In MF, both SIF and PI matched the spring onset and

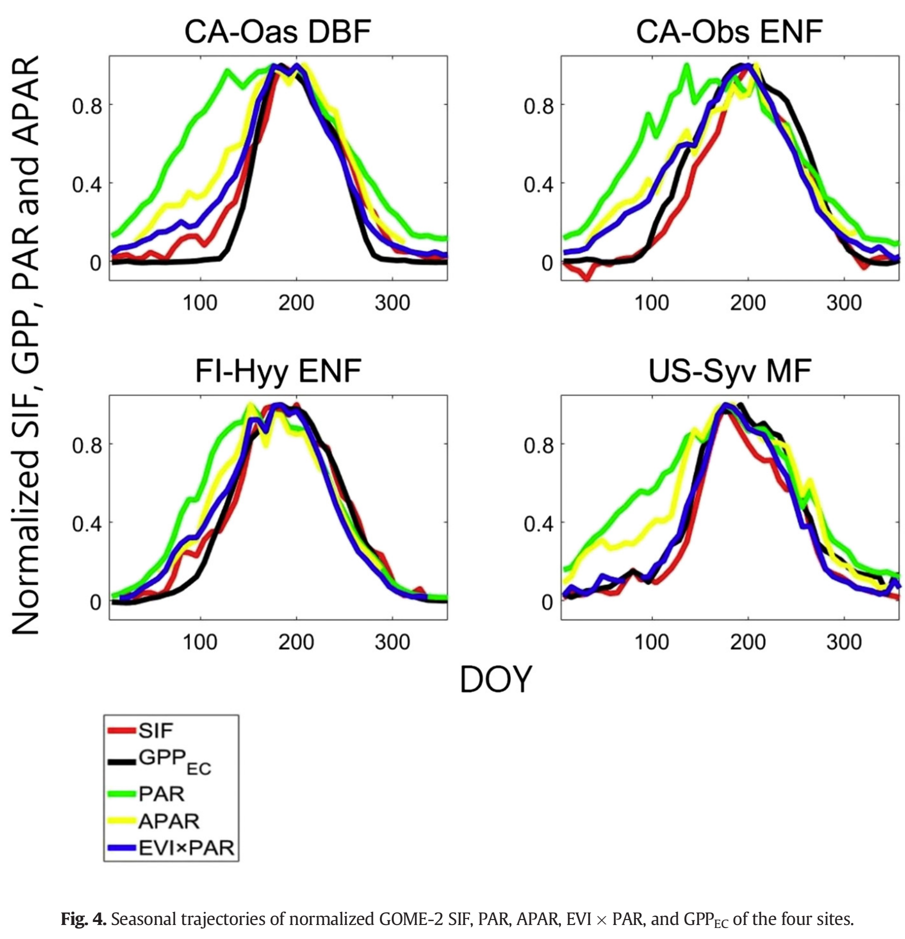

Fig. 4. Seasonal trajectories of normalized GOME-2 SIF, PAR, APAR, EVI × PAR, and GPP_{EC} of the four sites.

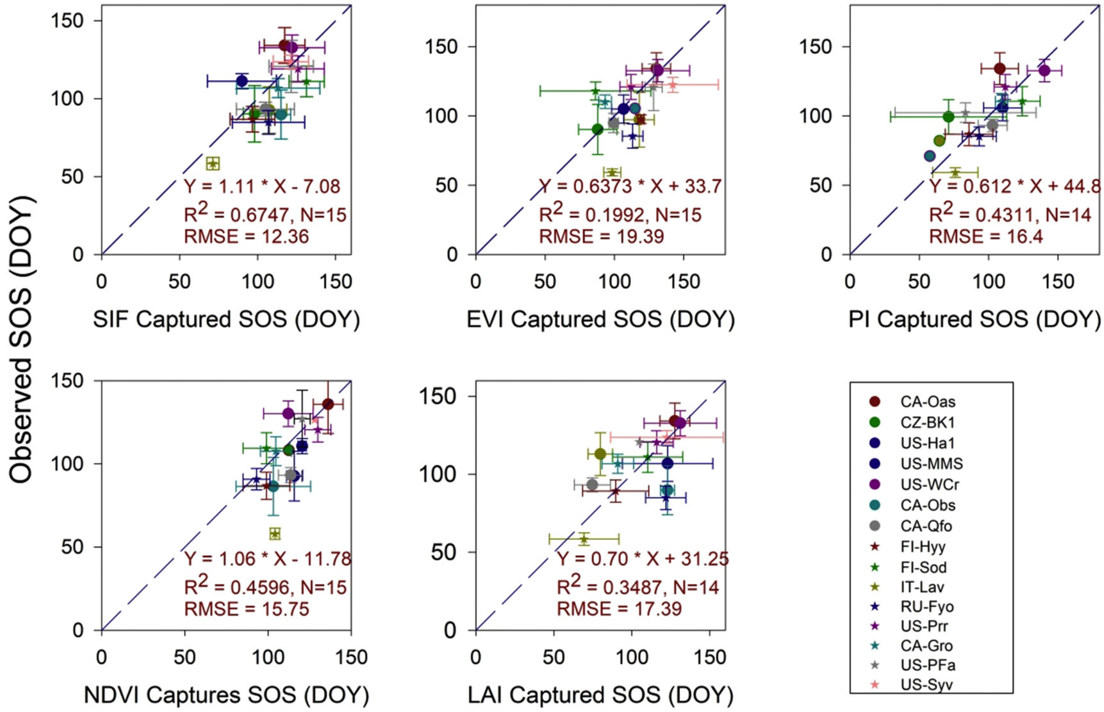

Fig. 5. Relationship between remotely sensed SOS and observed photosynthesis metrics determined by EC measurements. The equations and correlation coefficients of determination are shown. The number of sites used (N) and the RMSEs of the linear regressions are also provided for each site, and the error bars are the standard deviations of interannual variations. The absence of error bars indicates that the approaches shared only one year of retrievals, and dashed lines represent the 1:1 lines.

autumn senescence/abscission. For both ENF and DBF, MODIS LAI yielded shorter growing seasons possibly due to consistent biases.

We found that OCO-2 SIF captured phenological metrics were generally close to that of GPP_{EC} (Fig. 8). For most sites, OCO-2 SIF captured SOS and EOS matched closely with EC-based estimations, with the onset of spring and autumn within around 10 days. However, the OCO-2 inferred growing seasons were generally shorter than that inferred by GPP_{EC}. At some cases, yet, the seasonal cycles fitted by the double-logistic curve fitting methods were not consistent exactly with that of GPP_{EC} (see US-WCr).

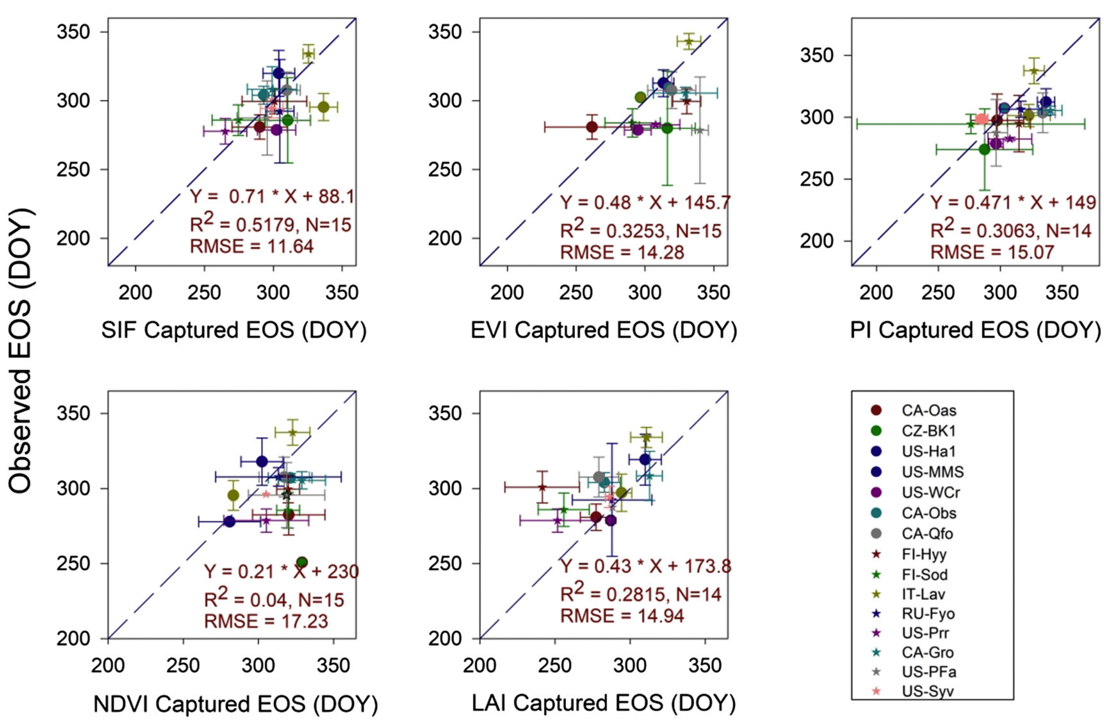

Fig. 6. Relationship between remotely sensed EOS and observed photosynthesis metrics determined by EC measurements. The equations and correlation coefficients of determination are shown. The number of sites used (N) and the RMSEs of the linear regressions are also provided for each site, and the error bars are the standard deviations of interannual variations. The absence of error bars indicates that the approaches shared only one year of retrievals, and dashed lines represent the 1:1 lines.

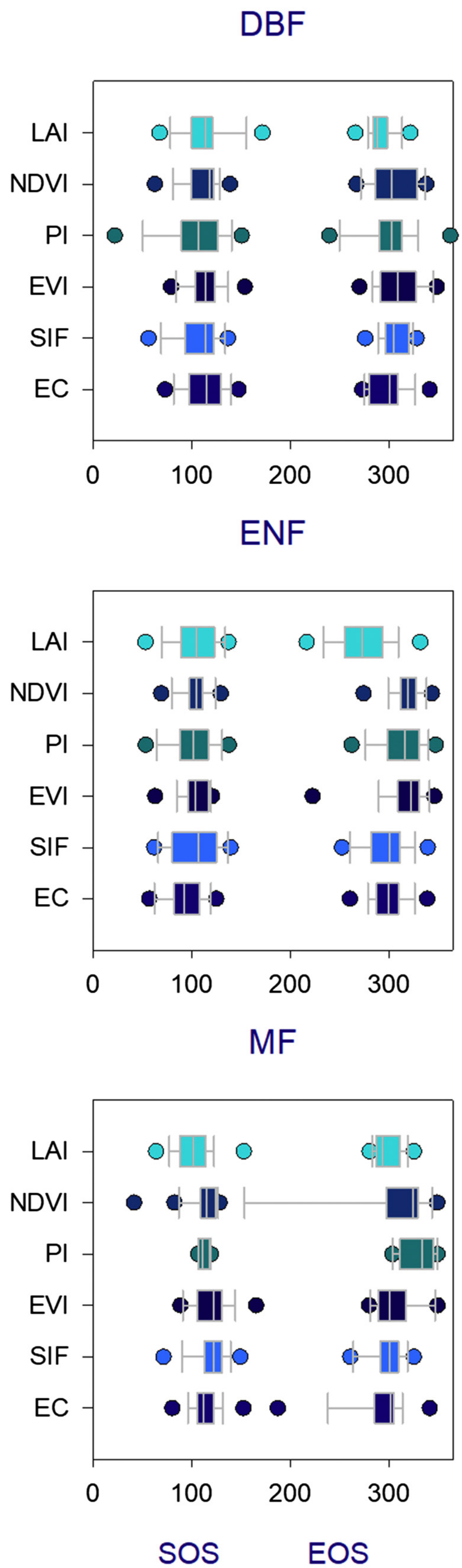

Fig. 7. The start and end of the growing seasons determined by different remote sensing measurements and EC measurements. For each data source, the central mark represents the median values, the edges of the box are the 25th and 75th percentiles, and the whiskers extend to the most extreme data points, i.e., 5th and 95th percentiles that were not considered.

4. Discussions

4.1. SIF-GPP relationship

In this study, we focused on 15 EC sites in mid-to-high latitude forests to examine the seasonal trajectories of satellite-derived VIs, LAI, and SIF, as well as their relationships with EC-based estimations of canopy photosynthesis. An additional objective was to explore the capacities of five remote sensing based measurements to track the key seasonal metrics in photosynthesis.

Despite the potentials of SIF to estimate GPP at various spatial and temporal scales, the SIF-GPP relationship can be complex and ecosystem-specific (Damm et al., 2015). Their relationship may contain the information of canopy structure as well as the physiological processes (Badgley et al., 2017). Several studies proposed that the use of a nonlinear model may be more appropriate in some cases due to the principle effects of non-photosynthetically quenching (NPQ) (Damm et al., 2010). Zhang et al. (2016a) found that SIF tended to be nonlinearly related to GPP at instantaneous scale, however, their relationship tended to linearize on daily to seasonal scales. Conversely, Verma et al. (2017) tested the SIF-GPP relationship at a grassland in Australia and pointed out that they found robust linear relationship even at instantaneous scale. In this study, we found that at instantaneous scale, the linear and hyperbolic models have similar performances. At the 16-day scales, the SIF-GPP relationship can generally be regarded as linear and the use of hyperbolic models may not help explain the relationship. Generally, we did not find significant nonlinear effects of NPQ especially at the 16-day scale. Yet, it needs to be addressed that there are two free parameters in the linear model and only one free parameter that need to be determined.

On seasonal scale, we compared the patterns in averaged GPP_{EC}, SIF and APAR of 15 EC sites and found close match between SIF and GPP_{EC} (Fig. 9). While SIF was a direct response to absorbed radiation, the fact that we found SIF and APAR had distinct seasonal cycles may suggest that SIF of mid-to-high latitude forests was not only driven by APAR but may also be affected by other factors (i.e., light use efficiency). Similar results were found in Walther et al. (2016). However, there are alternative possible explanations of the results that need to be addressed here. Firstly, since we used estimated daily SIF against the MODIS based estimations that are usually observed at instantaneous scale. This protocol may affect the results, although VIs of a canopy showed less significant variations within a day (Zhang et al., 2018). Secondly, the models that we used to estimate APAR may also impact the results. Relatively, EVI proxied APAR (EVI × PAR) showed a seasonal pattern more consistent with SIF and GPP_{EC} (Turner et al., 2003; Xiao et al., 2004b). These results were in line with previous results that found EVI being a better proxy of the fraction of chlorophyll absorbed PAR (Liu et al., 2017; Sims et al., 2008).

In summary, our results indicated that SIF-GPP relationship can generally be expressed by linear model and might contain information of APAR and LUE at 16-day scale. Thus, in theory, SIF, as an indicator that closely related to the photosynthesis processes, had great potentials for providing reliable estimations of dynamics of canopy photosynthesis, especially the seasonalities (Köhler et al., 2018; Walther et al., 2016). Although there are several light use efficiency models that exploit VIs to estimate GPP, SIF may serve as constrains or in the place of VIs to further evaluate their performances (Luus et al., 2017). Furthermore, it is also possible to develop empirical or process-based models based on the applications of SIF in a direction that may lead to more reliable estimations (Alemohammad et al., 2017).

4.2. Intercomparison of satellite captured seasonal patterns of canopy photosynthesis

In this study, we compared the potentials of five remote sensing based measurements in predicting seasonal trajectories of canopy

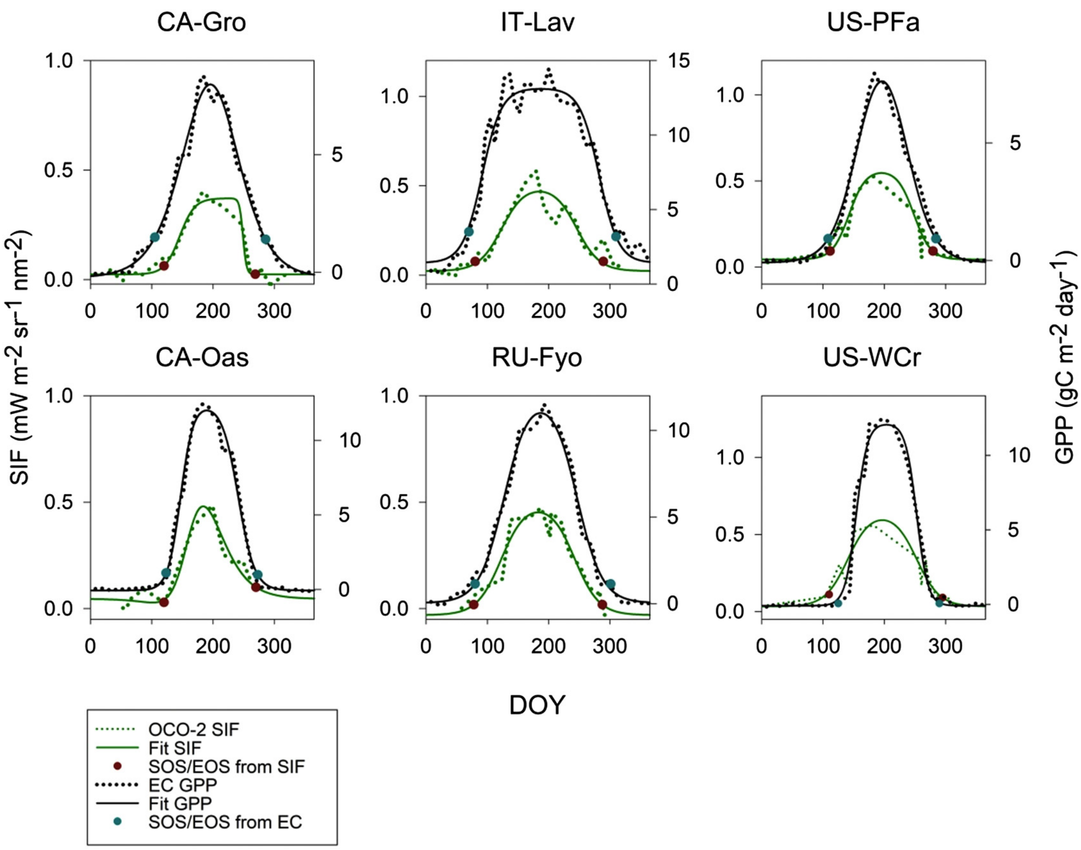

Fig. 8. The original EC GPP and OCO-2 SIF with the fitted seasonal cycles and predicted SOS and EOS at six forest sites.

photosynthesis. Remote sensing based approaches to determine phenological metrics (e.g., SOS and EOS) can be challenging because different parameters may respond uniquely to biophysical environments, resulting in different predictions. We found that, despite the mismatched spatial representativeness of GOME-2 SIF and mismatched observing time of OCO-2 SIF, the seasonal trajectories and phenological metrics depicted by these emerging SIF measurements matched closely with EC-based estimations.

The growing seasons of mid-to-high latitude forests were sensitive to climate variables. They control the exchanges of gases including CO_2 and trace gases such as O_3 (Anav et al., 2017). In our study, we found that satellite-derived SIF provided most reliable estimations of GPP-based seasonalities. VIs based estimations, however, were generally hindered in high-latitude areas possibly due to snow and soil moisture (Helman, 2018). For the populations in high-latitude regions, the growth (including photosynthesis) was restricted to a very short time window every annual cycle. Thus, to use SIF to constrain the models to estimate the seasonalities of photosynthesis would be extremely beneficial considering the short time window.

Regardless of our efforts in modelling seasonal cycles from two-year merged sets, the OCO-2 SIF measurements remained limited for most sites. At site-level, the limited numbers of observations would make it extremely difficult to reconstruct seasonal cycles of all sites because only very few sites had sufficient times of observations (Lu et al., 2018). The shortage of data may also be responsible for the relatively shorter growing seasons than that estimated by GPP_{EC} because the weight-based curving fitting method was hindered from determining the free parameters. Thus, at large scales, several studies attempted to generate the monthly means of OCO-2 SIF as the seasonal indicators (Köhler et al., 2018; Luus et al., 2017). The applications of OCO-2 SIF with relatively fine resolutions yet sparse coverages should be carefully deliberated.

4.3. Uncertainties and limitations

The uncertainties and limitations of the results were mainly attributed to the following two aspects.

Firstly, the imperfect match of spatial or temporal representativeness of satellite observations and EC estimations might affect the results. We acknowledged the inherent difficulties when comparing the relatively small spatial scales of tower-based estimations with those of the coarse resolutions of GOME-2 SIF. Although we selected sites with relatively homogenous forests, our assumption that the flux sites can represent the biophysical environment and vegetation of the whole girds might hinder the outcome and reliability of our work (Zhang et al., 2016a). Consequently, we used the upscaled GPP that matched the spatial scales of the GOME-2 SIF data as references and explored the emerging OCO-2 SIF at significant improved spatial resolutions that are similar to EC-based estimations (Verma et al., 2017). While the improved spatial representativeness of OCO-2 measurements, the sparse spatial resampling strategy and masks of cloudy measurements lead to limited observations for most sites, which makes it hard to apply them for retrieving seasonal patterns. In this study, we examined and proposed a 2-year (or 3-year) merges of remotely sensed fluorescence from OCO-2 to reconstruct the time series of a year by the corresponding day of the year of the measurements and to analyse the shifts of seasonal photosynthesis patterns based on them.

Secondly, optical remote sensing in high latitudes was relatively hindered. Influences of high sun-zenith angles, atmospheric effects and snow cover in the visible bands are obvious and the observations are often complicated by persistent cloud cover. Hence we used the MODIS nadir BRDF adjusted reflectance products in this study because it provided the estimations that are normalized to nadir, cloud-free, and atmospherically corrected.

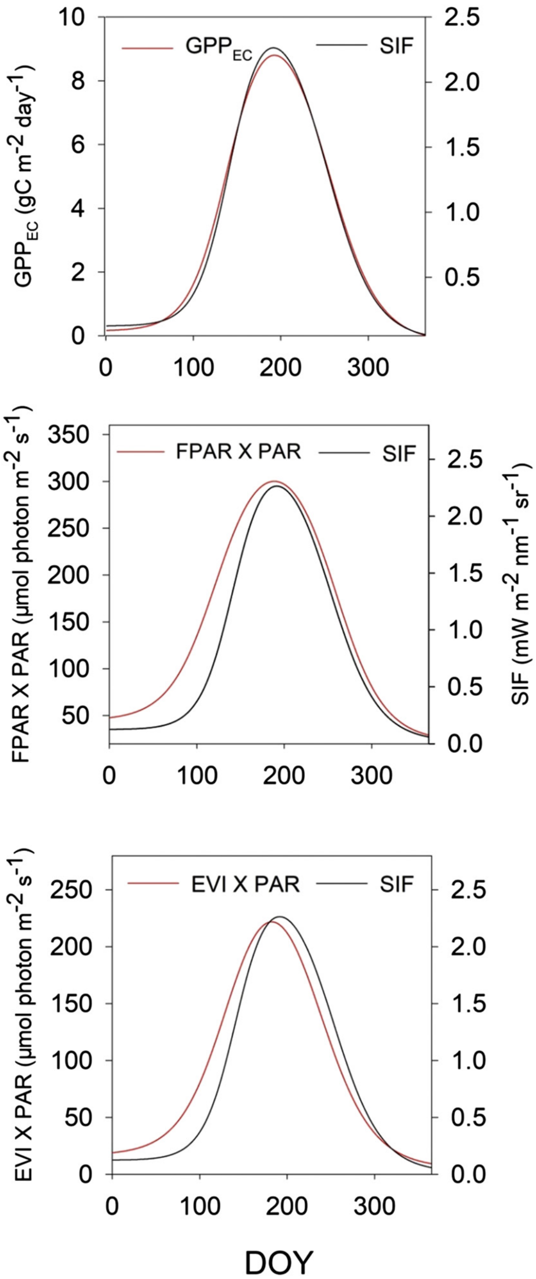

Fig. 9. The seasonal cycles of GPP_{EC}, GOME-2 SIF and two estimations of APAR by averaging the outcomes of all sites.

5. Conclusions and outlooks

Our results added additional endorsements for the applications of satellite-derived SIF in phenological studies in forest biomes. In 15 mid-to-high latitude forests in North America and Europe, the seasonal trajectories of GOME-2 datasets were significantly correlated with GPP_{EC} with R^2 values ranged from 0.52 to 0.74 with the linear model, while that ranged from 0.54 to 0.74 with the hyperbolic model. At the same time, the start and end of growing seasons estimated by GOME-2 and OCO-2 SIF matched closely with EC based estimations. Among MODIS estimations, the SOS captured by NDVI and PI were most reliable estimations with the R^2 over 0.4. No MODIS indexes accurately predicted the EOS with an overall R^2 below 0.3.

To sum up, we found that the relationship between SIF and GPP are generally linear on the 16-day scale and their relationship may contain additional information of LUE. As a result, the phenological metrics derived from SIF were consistent with EC based estimations. Due to the highly correlated SIF-GPP relationship and their similar seasonal cycles, the advantages of SIF can be exploited in the estimations of many photosynthesis related processes including phenology and gas exchanges. However, the applications of SIF were still challenged by the technical aspects at global scales at this moment. The spatial resolutions of GOME-2 SIF data make it hard to monitor the dynamics of photosynthesis at small scales. Recently, data from OCO-2 has the great potentials in advancing the estimations of regional photosynthesis. However, we found that growing seasons estimated by OCO-2 SIF were relatively shorter than that of the EC-based estimations (up to 3 to 4 weeks) possibly due to the limited data from OCO-2 SIF data for most sites. The limited observations from OCO-2 may lead its applications to be restrained at a small range of sites. Meanwhile, Tropospheric Monitoring Instrument (TROPOMI) that just recently launched on-board Sentinel-5 Precursor in October of 2017 and Fluorescence Explorer (Flex) scheduled to be launched around 2022 will start to provide global consistent observations soon. They will provide high-resolution global estimations of SIF (7 km by 7 km for TROPOMI and 300 m for Flex) that can be used to explore the potential of satellite-derived SIF in estimating photosynthetic capacity and seasonality (Frankenberg et al., 2014; Guanter et al., 2015; Rascher et al., 2008).

Supplementary data to this article can be found online at https://doi.org/10.1016/j.scitotenv.2018.06.269.

Acknowledgments

This work was supported by the Chinese Arctic and Antarctic Administration, National Natural Science Foundation of China, the Chinese Polar Environment Comprehensive Investigation, Assessment Program (Grant No. 41676176 and No. 41676182). This work was also supported by the Fundamental Research Funds for the Central Universities (Grant No. 312231103). We acknowledge Dr. Köhler P. for sharing the satellite-derived SIF, Dr. Tramontana G. and Prof. M. Jung for providing the upscaled model GPP. The data of OCO-2 SIF was produced by the OCO-2 project at the Jet Propulsion Laboratory, California Institute of Technology, and obtained from the OCO-2 data archive maintained at the NASA Goddard Earth Science Data and Information Services Center. Eddy based canopy measurements are from European Fluxes Database Cluster (http://gaia.agraria.unitus.it/) and Fluxnet (http://fluxnet.fluxdata.org/); we would like to address our appreciation for the PIs and staff that are working on these sites. The study of US-Syv, US-PFa, and Us-WCr is found by Department of Energy Office of Science, Ameriflux Network Management Project Support for UW ChEAS Cluster (2012–present). The study of US-Prr was supported by the JICS (JAMSTEC-UAF/IARC Collaboration Study). The data of this study can be access through figshare: https://doi.org/10.6084/m9.figshare.6709490.

References

Alemohammad, S.H., et al., 2017. Water, Energy, and Carbon with Artificial Neural Networks (WECANN): a statistically based estimate of global surface turbulent fluxes and gross primary productivity using solar-induced fluorescence. Biogeosciences 14 (18), 4101.

Anav, A., et al., 2017. The role of plant phenology in stomatal ozone flux modelling. Glob. Chang. Biol. 24 (1), 235.

Attard, K.M., Hancke, K., Sejr, M.K., Glud, R.N., 2016. Benthic primary production and mineralization in a High Arctic fjord: in situ assessments by aquatic eddy covariance. Mar. Ecol. Prog. Ser. 554, 35–50.

Badgley, G., Field, C.B., Berry, J.A., 2017. Canopy near-infrared reflectance and terrestrial photosynthesis. Sci. Adv. 3 (3), e1602244.

Baker, N.R., 2008. Chlorophyll fluorescence: a probe of photosynthesis in vivo. Annu. Rev. Plant Biol. 59 (1), 89–113.

Baldocchi, D., et al., 2001. FLUXNET: a new tool to study the temporal and spatial variability of ecosystem-scale carbon dioxide, water vapor, and energy flux densities. Bull. Am. Meteorol. Soc. 82 (82), 2415–2434.

Barr, A.G., et al., 2002. Comparing the carbon budgets of boreal and temperate deciduous forest stands. Can. J. For. Res. 32 (5), 813–822 (10).

Beer, C., et al., 2010. Terrestrial gross carbon dioxide uptake: global distribution and covariation with climate. Science 329 (5993), 834–838.

Bergeron, O., et al., 2007. Comparison of carbon dioxide fluxes over three boreal black spruce forests in Canada. Glob. Chang. Biol. 13 (1), 89–107.
Bond-Lamberty, B., Wang, C., Gower, S.T., 2004. A global relationship between the heterotrophic and autotrophic components of soil respiration? Glob. Chang. Biol. 10 (10), 1756–1766.
Buitenwerf, R., Rose, L., Higgins, S.I., 2015. Three decades of multi-dimensional change in global leaf phenology. Nat. Clim. Chang. 5 (4), 364–368.
Burrows, M.T., et al., 2011. The pace of shifting climate in marine and terrestrial ecosystems. Science 334 (6056), 652.
Chen, B., et al., 2012. Characterizing spatial representativeness of flux tower eddy-covariance measurements across the Canadian Carbon Program Network using remote sensing and footprint analysis. Remote Sens. Environ. 124 (124), 742–755.
Cleland, E.E., Chuine, I., Menzel, A., Mooney, H.A., Schwartz, M.D., 2007. Shifting plant phenology in response to global change. Trends Ecol. Evol. 22 (7), 357–365.
Cook, B.D., et al., 2004. Carbon exchange and venting anomalies in an upland deciduous forest in northern Wisconsin, USA. Agric. For. Meteorol. 126 (3–4), 271–295.
Dahlin, K., Fisher, R., Lawrence, P., 2015. Environmental drivers of drought deciduous phenology in the Community Land Model. Biogeosciences 12 (16), 5061–5074.
Damm, A., et al., 2010. Remote sensing of sun-induced fluorescence to improve modeling of diurnal courses of gross primary production (GPP). Glob. Chang. Biol. 16 (1), 171–186.
Damm, A., et al., 2015. Far-red sun-induced chlorophyll fluorescence shows ecosystem-specific relationships to gross primary production: an assessment based on observational and modeling approaches. Remote Sens. Environ. 166, 91–105.
Delbart, N., Kergoat, L., Toan, T.L., Lhermitte, J., Picard, G., 2005. Determination of phenological dates in boreal regions using normalized difference water index. Remote Sens. Environ. 97 (1), 26–38.
van der Tol, C., Berry, J.A., Campbell, P.K., Rascher, U., 2014. Models of fluorescence and photosynthesis for interpreting measurements of solar-induced chlorophyll fluorescence. J. Geophys. Res. Biogeosci. 119 (12), 2312–2327.
Desai, A.R., 2014. Influence and predictive capacity of climate anomalies on daily to decadal extremes in canopy photosynthesis. Photosynth. Res. 119 (1), 31–47.
Desai, A.R., Bolstad, P.V., Cook, B.D., Davis, K.J., Carey, E.V., 2005. Comparing net ecosystem exchange of carbon dioxide between an old-growth and mature forest in the upper Midwest, USA. Agric. For. Meteorol. 128 (1–2), 33–55.
D'Odorico, P., et al., 2015. The match and mismatch between photosynthesis and land surface phenology of deciduous forests. Agric. For. Meteorol. 214–215, 25–38.
Dragoni, D., et al., 2011. Evidence of increased net ecosystem productivity associated with a longer vegetated season in a deciduous forest in south-central Indiana, USA. Glob. Chang. Biol. 17 (2), 886–897.
Frankenberg, C., et al., 2011. New global observations of the terrestrial carbon cycle from GOSAT: patterns of plant fluorescence with gross primary productivity. Geophys. Res. Lett. 38 (17).
Frankenberg, C., et al., 2014. Prospects for chlorophyll fluorescence remote sensing from the Orbiting Carbon Observatory-2. Remote Sens. Environ. 147, 1–12.
Fretwell, P.T., et al., 2012. An emperor penguin population estimate: the first global, synoptic survey of a species from space. PLoS One 7 (4), e33751.
Gonsamo, A., Chen, J.M., 2016. Circumpolar vegetation dynamics product for global change study. Remote Sens. Environ. 182, 13–26.
Gonsamo, A., Chen, J.M., Price, D.T., Kurz, W.A., Wu, C., 2012a. Land surface phenology from optical satellite measurement and CO2eddy covariance technique. J. Geophys. Res. Biogeo. 117 (G3).
Gonsamo, A., Chen, J.M., Wu, C., Dragoni, D., 2012b. Predicting deciduous forest carbon uptake phenology by upscaling FLUXNET measurements using remote sensing data. Agric. For. Meteorol. 165, 127–135.
Guanter, L., et al., 2013. Using field spectroscopy to assess the potential of statistical approaches for the retrieval of sun-induced chlorophyll fluorescence from ground and space. Remote Sens. Environ. 133, 52–61.
Guanter, L., et al., 2014. Global and time-resolved monitoring of crop photosynthesis with chlorophyll fluorescence. Proc. Natl. Acad. Sci. U. S. A. 111 (14), E1327–E1333.
Guanter, L., et al., 2015. Potential of the TROPOspheric Monitoring Instrument (TROPOMI) onboard the Sentinel-5 Precursor for the monitoring of terrestrial chlorophyll fluorescence. Atmos. Meas. Tech. 8 (3), 1337–1352.
Helman, D., 2018. Land surface phenology: what do we really 'see' from space? Sci. Total Environ. 618, 665–673.
Huete, A., et al., 2002. Overview of the radiometric and biophysical performance of the MODIS vegetation indices. Remote Sens. Environ. 83 (1–2), 195–213.
Jeong, S.J., et al., 2017. Application of satellite solar-induced chlorophyll fluorescence to understanding large-scale variations in vegetation phenology and function over northern high latitude forests. Remote Sens. Environ. 190, 178–187.
Jin, C., et al., 2015. Effects of in-situ and reanalysis climate data on estimation of cropland gross primary production using the Vegetation Photosynthesis Model. Agric. For. Meteorol. 213, 240–250.
Joiner, J., et al., 2013. Global monitoring of terrestrial chlorophyll fluorescence from moderate-spectral-resolution near-infrared satellite measurements: methodology, simulations, and application to GOME-2. Atmos. Meas. Tech. 6 (10), 2803–2823.
Joiner, J., et al., 2014. The seasonal cycle of satellite chlorophyll fluorescence observations and its relationship to vegetation phenology and ecosystem atmosphere carbon exchange. Remote Sens. Environ. 152, 375–391.
Joiner, J., Yoshida, Y., Guanter, L., Middleton, E.M., 2016. New methods for retrieval of chlorophyll red fluorescence from hyper-spectral satellite instruments: simulations and application to GOME-2 and SCIAMACHY. Atmos. Meas. Tech. Discuss. 1–41.
Jung, M., Reichstein, M., Bondeau, A., 2009. Towards global empirical upscaling of FLUXNET eddy covariance observations: validation of a model tree ensemble approach using a biosphere model. Biogeosciences 6 (10), 2001–2013.
Jung, M., et al., 2011. Global patterns of land-atmosphere fluxes of carbon dioxide, latent heat, and sensible heat derived from eddy covariance, satellite, and meteorological observations. J. Geophys. Res. Biogeo. 116 (G3), 245–255.
Keenan, T.F., et al., 2014. Net carbon uptake has increased through warming-induced changes in temperate forest phenology. Nat. Clim. Chang. 4 (7), 598.
Köhler, P., Guanter, L., Joiner, J., 2015. A linear method for the retrieval of sun-induced chlorophyll fluorescence from GOME-2 and SCIAMACHY data. Atmos. Meas. Tech. 8 (6), 2589–2608.
Köhler, P., Guanter, L., Kobayashi, H., Walther, S., Yang, W., 2018. Assessing the potential of sun-induced fluorescence and the canopy scattering coefficient to track large-scale vegetation dynamics in Amazon forests. Remote Sens. Environ. 204, 769–785.
Li, X., Xiao, J., He, B., 2018. Chlorophyll fluorescence observed by OCO-2 is strongly related to gross primary productivity estimated from flux towers in temperate forests. Remote Sens. Environ. 204, 659–671.
Liu, Z., et al., 2017. Improved modeling of gross primary production from a better representation of photosynthetic components in vegetation canopy. Agric. For. Meteorol. 233, 222–234.
Loveland, T.R., et al., 2000. Development of a global land cover characteristics database and IGBP DISCover from 1 km AVHRR data. Int. J. Remote Sens. 21 (6–7), 1303–1330.
Lu, X., Xiao, C., Xianglan, L., Tang, J., 2018. Opportunities and challenges of applications of satellite-derived sun-induced fluorescence at relatively high spatial resolution. Sci. Total Environ. 619-620C, 649–653.
Luo, X., Chen, X., Wang, L., Xu, L., Tian, Y., 2014. Modeling and predicting spring land surface phenology of the deciduous broadleaf forest in northern China. Agric. For. Meteorol. 198-199, 33–41.
Luus, K.A., Lin, J.C., 2015. The Polar Vegetation Photosynthesis and Respiration Model: a parsimonious, satellite-data-driven model of high-latitude CO_2 exchange. Geosci. Model Dev. 8 (8), 2655–2674.
Luus, K.A., et al., 2017. Tundra photosynthesis captured by satellite-observed solar-induced chlorophyll fluorescence. Geophys. Res. Lett. 44 (3), 1564–1573.
Marcolla, B., Pitacco, A., Cescatti, A., 2003. Canopy architecture and turbulence structure in a coniferous forest. Bound.-Layer Meteorol. 108 (1), 39–59.
Mccaughey, J.H., Pejam, M.R., Arain, M.A., Cameron, D.A., 2006. Carbon dioxide and energy fluxes from a boreal mixedwood forest ecosystem in Ontario, Canada. Agric. For. Meteorol. 140 (1–4), 79–96.
Melaas, E.K., Wang, J.A., Miller, D.L., Friedl, M.A., 2016. Interactions between urban vegetation and surface urban heat islands: a case study in the Boston metropolitan region. Environ. Res. Lett. 11 (5), 054020.
Milyukova, I.M., et al., 2002. Carbon balance of a southern taiga spruce stand in European Russia. Tellus 54 (5), 429–442.
Myneni, R.B., et al., 2002. Global products of vegetation leaf area and fraction absorbed PAR from year one of MODIS data. Remote Sens. Environ. 83 (1–2), 214–231.
Nakai, T., et al., 2013. Characteristics of evapotranspiration from a permafrost black spruce forest in interior Alaska. Polar Sci. 7 (2), 136–148.
Peng, D., et al., 2017. Spring green-up phenology products derived from MODIS NDVI and EVI: intercomparison, interpretation and validation using National Phenology Network and AmeriFlux observations. Ecol. Indic. 77, 323–336.
Peñuelas, J., Rutishauser, T., Filella, I., 2009. Phenology feedbacks on climate change. Science 324 (5929), 887–888.
Rascher, U., Gioli, B., Miglietta, F., 2008. FLEX — Fluorescence Explorer: A Remote Sensing Approach to Quantify Spatio-Temporal Variations of Photosynthetic Efficiency from Space. Springer Netherlands, pp. 1387–1390.
Reichstein, M., et al., 2005. On the separation of net ecosystem exchange into assimilation and ecosystem respiration: review and improved algorithm. Glob. Chang. Biol. 11 (9), 1424–1439.
Rolleston, H.D., 1996. Influence of the temperate and boreal forests on the Northern Hemisphere climate in the Météo-France climate model. Clim. Dyn. 13 (13), 57–74.
Sims, D.A., et al., 2008. A new model of gross primary productivity for North American ecosystems based solely on the enhanced vegetation index and land surface temperature from MODIS. Remote Sens. Environ. 112 (4), 1633–1646.
Staudt, K., Foken, T., 2008. Documentation of Reference Data for the Experimental Areas of the Bayreuth Centre for Ecology and Environmental Research (BayCEER) at the Waldstein Site.
Sun, Y., et al., 2017. OCO-2 advances photosynthesis observation from space via solar-induced chlorophyll fluorescence. Science 358 (6360), eaam5747.
Sun, Y., et al., 2018. Overview of Solar-Induced chlorophyll Fluorescence (SIF) from the Orbiting Carbon Observatory-2: retrieval, cross-mission comparison, and global monitoring for GPP. Remote Sens. Environ. 209, 808–823.
Suni, T., Rinne, J., Reissell, A., Al, E., 2003. Long-term measurements of surface fluxes above a Scot pine forest in Hyytiälä southern Finland, 1996–2001. Boreal Environ. Res. 8 (4), 287–301.
Tanja, S., et al., 2003. Air temperature triggers the recovery of evergreen boreal forest photosynthesis in spring. Glob. Chang. Biol. 9 (10), 1410–1426.
Tramontana, G., et al., 2016. Predicting carbon dioxide and energy fluxes across global FLUXNET sites with regression algorithms. Biogeosci. Discuss. 13 (14), 1–33.
Turner, D.P., et al., 2003. Scaling Gross Primary Production (GPP) over boreal and deciduous forest landscapes in support of MODIS GPP product validation. Remote Sens. Environ. 88 (3), 256–270.
Urbanski, S., et al., 2007. Factors controlling CO2 exchange on timescales from hourly to decadal at Harvard Forest. J. Geophys. Res. Biogeo. 112 (G2), 225–236.
Verma, M., et al., 2017. Effect of environmental conditions on the relationship between solar-induced fluorescence and gross primary productivity at an OzFlux grassland site. J. Geophys. Res. Biogeo. 122 (3).
Viña, A., Liu, W., Zhou, S., Huang, J., Liu, J., 2016. Land surface phenology as an indicator of biodiversity patterns. Ecol. Indic. 64, 281–288.

Walther, S., et al., 2016. Satellite chlorophyll fluorescence measurements reveal large-scale decoupling of photosynthesis and greenness dynamics in boreal evergreen forests. Glob. Chang. Biol. 22 (9), 2979–2996.

Wang, C., Cao, R., Chen, J., Rao, Y., Tang, Y., 2015. Temperature sensitivity of spring vegetation phenology correlates to within-spring warming speed over the Northern Hemisphere. Ecol. Indic. 50, 62–68.

Wang, G., et al., 2016. On the development of a coupled regional climate–vegetation model RCM–CLM–CN–DV and its validation in Tropical Africa. Clim. Dyn. 46 (1–2), 515–539.

Wong, C.Y., Gamon, J.A., 2015. The photochemical reflectance index provides an optical indicator of spring photosynthetic activation in evergreen conifers. New Phytol. 206 (1), 196.

Wu, C., et al., 2017. Land surface phenology derived from normalized difference vegetation index (NDVI) at global FLUXNET sites. Agric. For. Meteorol. 233, 171–182.

Xiao, X., et al., 2004a. Satellite-based modeling of gross primary production in an evergreen needleleaf forest. Remote Sens. Environ. 89 (4), 519–534.

Xiao, X., et al., 2004b. Modeling gross primary production of temperate deciduous broadleaf forest using satellite images and climate data. Remote Sens. Environ. 91 (2), 256–270.

Yang, X., et al., 2015. Solar-induced chlorophyll fluorescence that correlates with canopy photosynthesis on diurnal and seasonal scales in a temperate deciduous forest. Geophys. Res. Lett. 42 (8), 2977–2987.

Yang, X., et al., 2016. Seasonal variability of multiple leaf traits captured by leaf spectroscopy at two temperate deciduous forests. Remote Sens. Environ. 179, 1–12.

Yang, H., et al., 2017. Chlorophyll fluorescence tracks seasonal variations of photosynthesis from leaf to canopy in a temperate forest. Glob. Chang. Biol. 23 (7), 2874–2886.

Zhang, Y., et al., 2016a. Model-based analysis of the relationship between sun-induced chlorophyll fluorescence and gross primary production for remote sensing applications. Remote Sens. Environ. 187, 145–155.

Zhang, Y., et al., 2016b. Consistency between sun-induced chlorophyll fluorescence and gross primary production of vegetation in North America. Remote Sens. Environ. 183, 154–169.

Zhang, Y., et al., 2018. On the relationship between sub-daily instantaneous and daily total gross primary production: implications for interpreting satellite-based SIF retrievals. Remote Sens. Environ. 205.

Zipper, S.C., et al., 2016. Urban heat island impacts on plant phenology: intra-urban variability and response to land cover. Environ. Res. Lett. 11 (5), 054023.